CHAPTER 3

Empirical and Process Studies

CDC's climate research effort has a firm foundation in empirical studies, consistent with our emphasis on climate monitoring, understanding and prediction. The science projects in this area involve not only seasonal to interannual time scales but also specifically target the annual cycle and intraseasonal variability. On interannual time scales the focus is on ENSO. Empirical studies at CDC have refined our understanding of the global circulation's response to ENSO SST anomalies as the diabatic forcing and the base state change with the annual cycle. These insights have prompted some of the modeling investigations described in section 3.1.

Several projects are devoted to advancing our knowledge of the annual cycle. The role of clouds in seasonal mass circulations is one area of interest, and preliminary work with different data sets shows that there is considerable room for improvement in the depiction of clouds in the NCEP reanalyses. Fundamental work is being carried out on representing convective clouds and precipitation in general circulation models by examining an equilibrated cloud ensemble's sensitivity to various forcings. Other areas being investigated include sudden transitions in the latitude of the jet stream, stratosphere-troposphere exchange, and seasonal base state controls on higher frequency variability.

CDC believes more research is required to understand the role of intraseasonal variability in seasonal climate anomalies. Seldom is boundary forcing strong enough to overcome the inherent noise in the atmosphere-ocean system, especially in mid-latitudes over North America where much of our diagnostic work is focused. Moreover, the prediction of extreme events such as floods, droughts, cold and warm spells, involves the synergistic effects of multiple time scales from synoptic to interannual. Intraseasonal time scales encompass a complex set of phenomena including coherent features, such as the Madden-Julian oscillation (MJO), teleconnection patterns and zonal index variations. The MJO in particular provides a focus for our studies on this time scale.

Our investigations of the MJO encompass both the atmosphere and ocean. The MJO is characterized by large-scale convective flare-ups that develop over the equatorial Indian Ocean every 30-60 days and then move slowly eastward toward the central Pacific. The wet phase of enhanced convection and precipitation is followed by a dry phase where convection is suppressed. A concerted effort is underway to diagnose and model the sea surface temperature anomalies that accompany the movement of convection across the IndoPacific region. The role of MJO activity in interannual variations of the monsoons in the IndoPacific region is also under investigation. Results of this study should shed light onto whether intraseasonal activity needs to be faithfully depicted for accurate simulation and forecast of these seasonal mean monsoons. The extension of the signal of the MJO into mid-latitudes is also being investigated, with emphasis on both the zonal mean and eddy components.

While scientific understanding remains a strong motivation, CDC also emphasizes a real time awareness of the observed climate through weekly weather meetings and virtual and hardcopy maprooms. These meetings provide an arena for discussing and exchanging ideas on evolving low frequency events including ENSO, the annual cycle, MJOs, zonal index variations, storm tracks, etc.

3.1 Annual climate and annual cycle

3.1.1 The role of clouds for the seasonal cycle in the equatorial east Pacific

Clouds play an important role in global climate. They exert a strong influence on the mean state and variability of the atmosphere and ocean. Inaccurate simulations of cloud properties in general circulation models (GCMs) are a leading cause of errors in simulations of the Earth's climate. CDC is exploring the role of clouds for the seasonal cycle of atmosphere and ocean variability in the east Pacific as part of the Pan American Climate Studies program.

To that end, radiative heating rates in the atmosphere have been calculated using the radiative transfer model of the NCAR CCM3 general circulation model. Temperature and humidity data from ECMWF analyses and observed cloud properties from the International Satellite Cloud Climatology Project serve as inputs to the radiative transfer model.

Top-of-the-atmosphere fluxes agree well with observations from the Earth Radiation Budget Experiment and surface fluxes agree well with the GEWEX Surface Radiation Budget. Thus the calculation provides an accurate assessment of the seasonal and interannual variations of radiative heating in the atmosphere. The calculated fluxes and heating rates are examined for the impact of clouds on energetics at the surface and in the atmosphere and also form the basis for evaluating the NCEP/NCAR reanalysis data. In addition, by driving diagnostic models of the ocean and atmospheric circulations with the calculated fluxes and heating rates, the impact of clouds on those circulations will subsequently be quantified.

The impact of clouds on the seasonal cycle of radiative energy fluxes at the surface is illustrated in **Fig. 3.1a**, which displays the amplitude of the annual harmonic of cloud radiative forcing (CRF) at the surface in the east Pacific. CRF is the difference between two flux calculations: one including cloud properties and the other omitting them. Clouds exert a strong influence on the annual amplitude of surface flux at convective locations over the South Pacific, the intertropical convergence zone, the Amazon basin, and at subtropical subsidence/stratus locations in the northeast and southeast Pacific. The contribution by clouds in those regions represents 20-50% of the seasonal cycle of the net surface energy flux. **Fig. 3.1b** shows the amplitude of the annual harmonic of the difference between surface fluxes calculated from observed cloud properties and surface fluxes from the NCEP/NCAR reanalysis data. That difference quantifies the impact of cloud field errors in NCEP reanalysis on the seasonal cycle of surface fluxes. That impact is largest over locations dominated by low stratus and stratocumulus clouds. For example, the error in surface flux over the equatorial cold tongue is as large as the annual amplitude of net surface energy flux there.

3.1.2 Parameterization of convective clouds

Ensembles of convective clouds participate in "moist" tropical circulations ranging from hurricanes to easterly waves to monsoons to ENSO. The

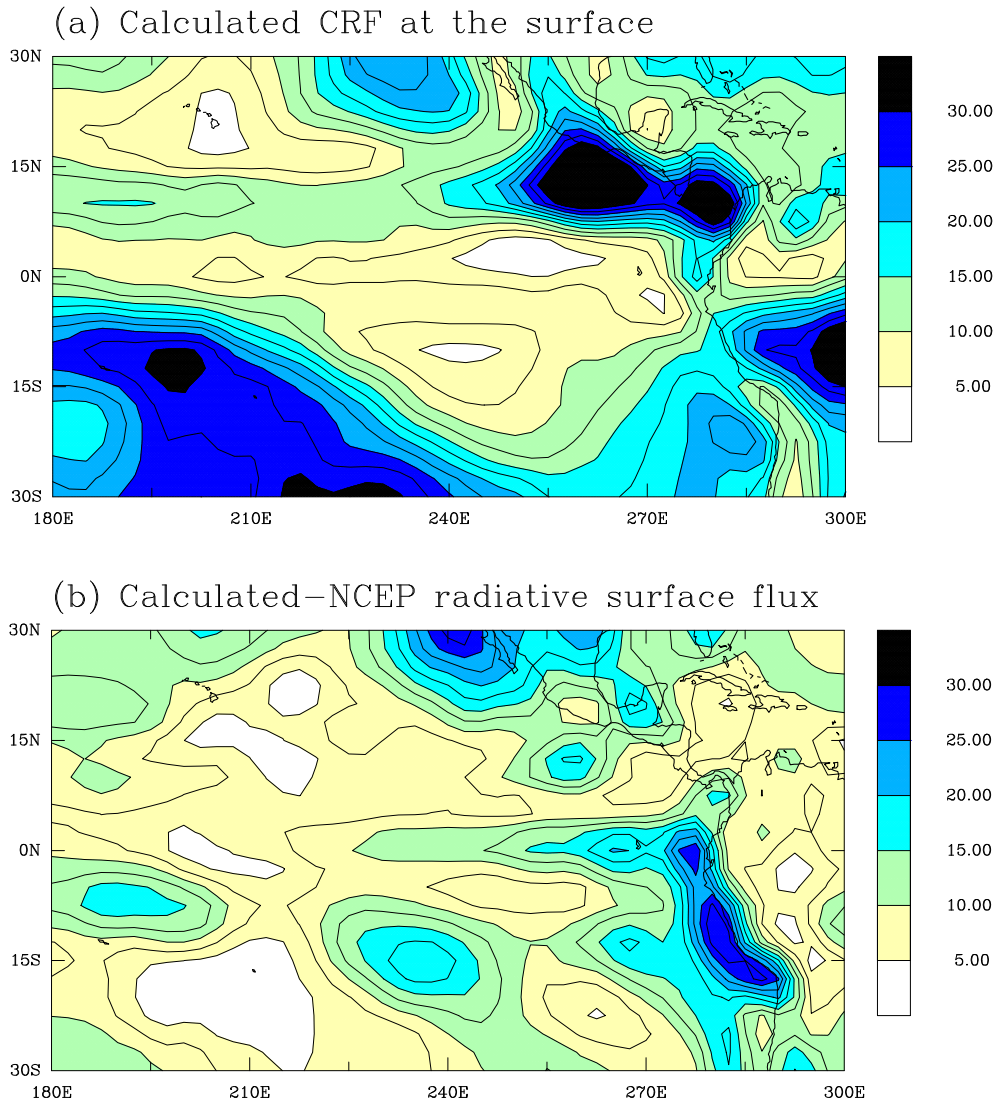

Fig. 3.1. The amplitude of the first annual harmonic of (a) calculated cloud radiative forcing (CRF) at the surface and (b) the difference between calculated and NCEP surface fluxes in the east Pacific.

cumulus parameterization problem consists of specifying the bulk sensitivities of these ensembles: outputs (e.g. condensation rate) as a function of inputs. Current computer power permits explicit simulation of multiple clouds for multiple cloud lifetimes. It should be possible to begin mapping the sensitivities of these ensembles. The key to such cumulus ensemble sensitivity modeling studies is developing a model strategy under which the modeled cloud ensemble is not controlled by lateral boundary conditions ("forcing") or initial conditions.

We first obtain a control simulation involving an ensemble of clouds of vari-

ous sizes in a statistical steady state, equilibrated with their environmental stratification (**Fig. 3.2**). Because **Fig. 3.2** was obtained with periodic lateral boundary conditions and artificial forcing, some modification is needed to restore the domain to the basic thermodynamic balance found in natural cloud ensembles.

The sensitivity of this cumulus ensemble to a variety of observationally-derived perturbations will be computed. These perturbations include environmental density perturbations, humidity changes such as "dry tongues", and wind shear changes of the kinds observed in tropical sounding data. The most systematic of these sensitivities will be incorporated into new cumulus parameterizations for GCMs. Most current schemes have little or no sensitivity to convective inhibition, or to dry air aloft. No current schemes have any sensitivity to wind shear. How much can improved convection schemes improve global weather and climate forecasts?

3.1.3 Abrupt changes in the annual cycle of the Northern Hemisphere jet streams

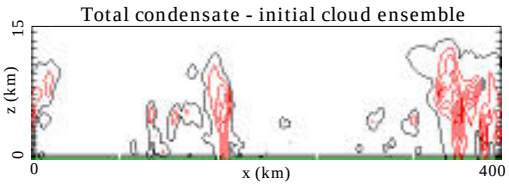

Fig. 3.2. GATE 12Z 13 September total condensate, from Grabowski et al (1996). The domain is laterally periodic, so several copies of this field can be used to increase ensemble size.

The annual cycle of the upper-tropospheric Asian and American jet streams directly impacts the annual cycle of precipitation in the United States. Documenting the annual cycle of the jet stream provides a basis for investigating its dynamics, comparing it with general circulation model climatologies and monitoring seasonal transitions in the circulation. The annual cycle of the climatological Asian and American jet streams is strongly asymmetric in time and shows abrupt changes, especially in the spring. **Fig. 3.3a** shows that during winter the axis of the Asian jet stream is anchored along 30˚N. The jet stream bifurcates abruptly in late March over the central-and-eastern North Pacific region, with the northern branch centered around 42˚N and the southern branch around 18˚N. After a split jet regime during northern summer, the jet moves gradually southward to its winter location in the autumn. The jet decelerates very quickly during March and accelerates rather slowly in the autumn.

The annual cycle of the climatological American jet stream looks like a saw-tooth wave (**Fig. 3.3b**). The center of the jet is in its northernmost position of about 45˚N in the summer. From September onward, the jet moves gradually southward until the end of May when it jumps abruptly northward by more than 20˚of latitude from about 23˚N to 45˚N. The jet stream is strongest in late January and weakest in early June. The jet decelerates very rapidly in May and accelerates fairly slowly in the autumn.

The bifurcation of the Asian jet stream in late March is associated with an abrupt shift in the precipitation pattern over the United States. **Fig. 3.4a** shows

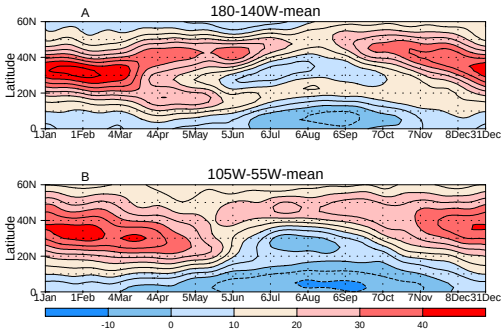

Fig. 3.3 Annual cycle of zonal wind at 200 mb. The contour interval is 5 m s^{-1}.

that west of the Rocky Mountains, precipitation is mainly confined to the latitude band of 32-40˚N in the winter and early spring. The precipitation band jumps abruptly northward by 10 degrees of latitude in early April, and remains there until the end of the summer. East of the Rocky Mountains (**Fig. 3.4b**), there is little precipitation in the winter and early spring. The rainy season arrives suddenly in early April throughout the latitude band from 30˚ to 50˚N, with the heaviest precipitation occurring in early June. In fact, heavy precipitation occurs throughout the Rocky Mountains along 45˚N in early June and corresponds to the abrupt northward jump of the American jet.

CDC scientists are currently investigating the role of tropical heating and wave breaking in these sudden transitions of the circulation during the annual cycle.

3.1.4 Isentropic stratosphere-troposphere exchange

The exchange of chemically and radiatively active trace gases, such as ozone and water vapor, between the stratosphere and troposphere alters the chemical and radiative balances in both regions, which would, in turn, influence the radiative forcing of the global climate system. A better understanding of the physics and dynamics of stratosphere-troposphere exchange (S/T exchange) is thus critical to understanding and predicting global climate change and assessing the climatic impacts of human activities.

Stratosphere-troposphere exchange along isentropic surfaces that intersect the extratropical tropopause has been investigated using a transport model driven by analyzed global winds. The characteristics of along-isentrope S/T exchange exhibit two distinctive regimes. At 330K and below, S/T exchange occurs vigorously in all seasons. At 340K and above, however, it has a strong annual cycle; very little exchange takes place in the winter hemisphere, but significant exchange occurs in the summer hemisphere, particularly during northern summer. As an example, the results from two experiments for the winter of 1992/1993 and the summer of 1993 on the 350 K isentropic surface are discussed here.

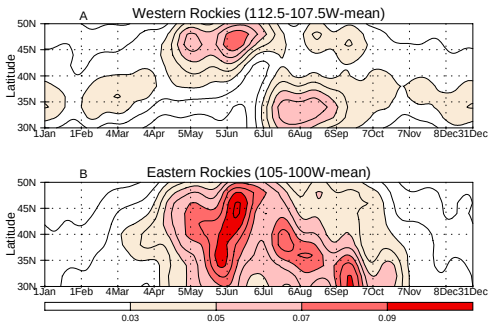

Fig. 3.4 Annual cycle of precipitation. The contour interval is 0.01 inches per day.

An idealized passive tracer that is zonally symmetric and entirely in the stratosphere is initialized on Nov. 1, 1992 in the winter experiment and on May 1, 1993 in the summer experiment. The tracer field is then advected by the 6-hourly nondivergent winds from the NCEP/NCAR reanalyses for four months. **Fig. 3.5** shows the tracer field and the 2 PVU potential vorticity contour on Feb. 28, 1993 and on Aug. 31, 1993. During the four winter months very little tracer has been transported from the stratosphere into the troposphere (upper panel). During the summer, on the other hand, a considerable amount of tracer has been transported from the stratosphere into the troposphere (lower panel). The weak wintertime S/T exchange is due to the strong barrier effects of the steep gradients of potential vorticity at the tropopause while the strong summertime S/T exchange is related to the transport and mixing by disturbances associated with the Asian and Mexico monsoon anticyclones.

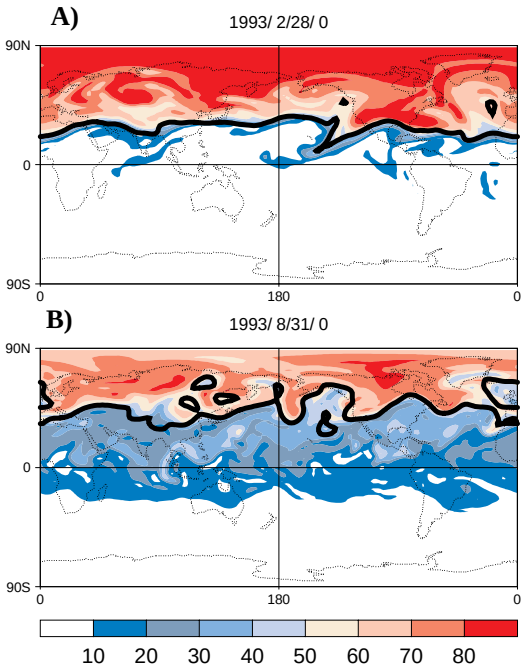

Fig. 3.5 Distribution of an idealized passive tracer on (A) Feb. 28, 1993 and (B) Aug. 31, 1993 after four months of integration in a transport model using analyzed winds. The heavy solid curve is the 2 PVU potential vorticity contour which marks roughly the tropopause.

3.1.5 Submonthly convection and circulation variations

The circulation changes associated with the annual cycle exert a strong influence on the character of submonthly variability of convection and circulation. Using ten years of outgoing longwave radiation (OLR) and circulation data, 6-30 day filtered variations were examined during the standard three-month seasons. Regression relationships between filtered OLR at various locations in the Tropics and the 200 and 850 mb circulation were mapped. **Fig. 3.6** presents a summary of the results. In regions where convection is embedded in base state upper-level easterlies, anomalous equatorial easterly flow is typically present at 200 mb within and to the west of the convective signal, along with patterns of meridional outflow into subtropical anticyclonic perturbations (**Fig. 3.6a** and **3.6b**). Lagged relationships suggest that the convection is forcing the circulation in these cases. As a contrast, in regions located within base state upper-level westerlies or along the margin of influence of upper westerly disturbances, convection appears to be forced by upper-level wave energy propagating into the deep Tropics, with the convective signal located in the upward motion region ahead of upper-level troughs (**Fig. 3.6c**). The results confirm theoretical and modeling ideas that suggest that Rossby wave energy is able to

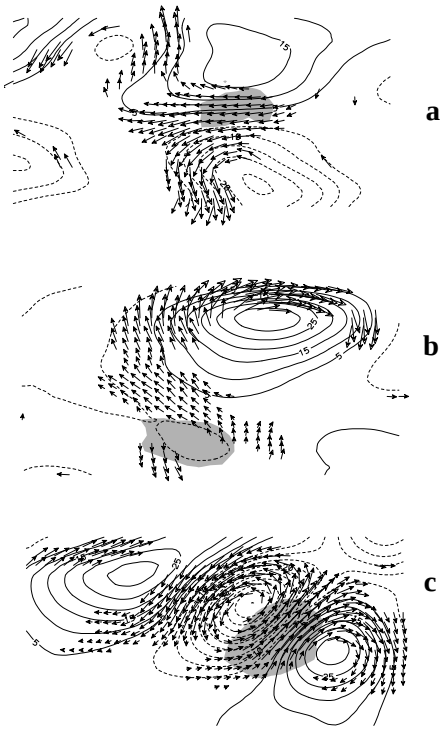

200-mb

a Near-equatorial convection embedded in anomalous easterly flow within and to the west of the heating, and linked to symmetric anticyclones in the subtropics of both hemispheres. Most common in equinoctial seasons. Propagates westward.

b Convection in summer hemisphere with cross-equatorial outflow into the winter hemisphere jet and anticyclone. Also occurs in conjunction with near-equatorial convection. Most common during solstitial seasons. Convection stationary, subtropical features propagate eastward.

c Convection ahead of an upper level trough associated with wave energy propagating into the tropics. Occurs primarily in regions of upper level westerlies at low latitudes. Indicative of forcing of the convection by wave activity at upper levels. Propagates eastward and equatorward.

Fig. 3.6. Summary figure of principal 200 mb modes of circulation associated with 6-30-day tropical convection. Shading denotes regions of negative OLR perturbations.

propagate into the deep Tropics in regions of upper-level westerlies.

3.2 Intraseasonal Variations

3.2.1 Madden-Julian oscillation: Tropical influences

Diagnostic studies of the atmospheric Madden-Julian oscillation (MJO) have concentrated on elucidating where and when the signal of the MJO is prominent. In general, the strongest eastward propagating anomalies of convection and circulation occur during December-April along the equator in the eastern hemisphere, where climatological convection and warmest SST occur at this time of year. The local zonal scale of the convective anomaly over the Indian and western Pacific oceans is about 7500km (~zonal wavenumber 2-3), such that while enhanced convection covers the Indian Ocean, suppressed convection covers the western Pacific. A half cycle later, when the enhanced convection has propagated into the western Pacific, the reverse occurs. Hence, the convective disturbance has the appearance of a standing oscillation. However, this apparent standing oscillation is better interpreted as the spatial modulation of a purely zonally propagating disturbance.

Thus, theories of the MJO, based on the assumption of a standing convective component that gives rise to a propagating circulation anomaly, appear not to be relevant. On the other hand, Hendon

and Salby 1994 emphasized the possible role of frictional wave CISK as the mechanism of the MJO, whereby frictional surface convergence some 30˚ to 40˚ longitude to the east of the inviscid lower tropospheric convergence fuels convection in-phase with the large-scale tropospheric temperature anomaly associated with the MJO.

Synoptic and higher frequency activity is important both for its rectified effect on seasonal time scales (i.e., the seasonal average of a given quantity would be different in the absence of these transients), and because day-to-day weather is often more significant to people than seasonal averages. Research has shown that synoptic and mesoscale convection is enhanced during the large-scale convectively active phase of the MJO. The increase occurs uniformly over all synoptic time-scales, but little difference in the character of the variability is observed between dry and wet phases.

Enhanced mesoscale activity within the active phase exhibits a marked tendency to be organized into westward propagating clusters with periods near 2 days and half wavelengths of about 1000 km. It is hypothesized that the local 2-day period results from a diurnal cycle of convective forcing that is farther to the east each day with the envelope of MJO activity, thus requiring an extra day for the westward propagating disturbance to return to the original longitude. Across the eastern hemisphere, the MJO provides large-scale conditions favorable for tropical cyclone development (**Fig. 3.7**). The idea that the MJO modulates tropical cyclone activity has been included in experimental intraseasonal prediction of tropical cyclones at the Darwin forecast office of the Australian Bureau of Meteorology.

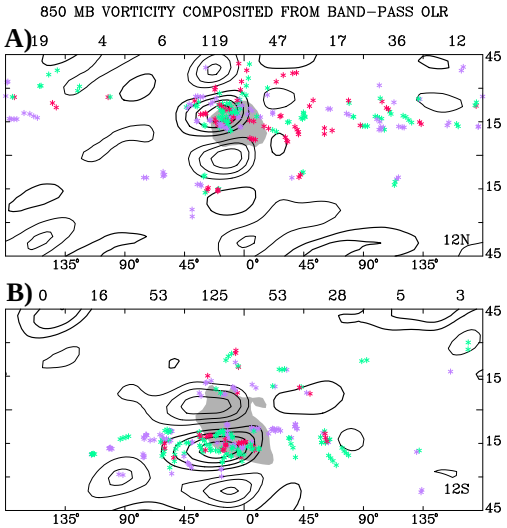

Fig. 3.7. Composite vorticity anomaly based on 35-95 day band-pass OLR anomalies between 60˚E and 180˚ that have been rotated to a relative longitude of 0˚ at (a) 12˚N and (b) 12˚S. Positive relative vorticity anomalies are thick in (a) and negative anomalies thick in (b). The contour interval is $5x10^{-7}s^{-1}$ with contours starting at $5x10^{-7}s^{-1}$. The vorticity fields have been band-pass filtered to include periods from 35-95 days and spatially truncated at T12. Shading represents composited filtered OLR anomalies of more than 7 Wm^{-2}. Asterisks represent reports of tropical disturbances of depression strength or greater, plotted relative to the OLR anomaly. The total number of cyclone reports in each 45˚ octant is written above each figure.

3.2.2 Madden-Julian oscillation: Extratropical influences

Circulation anomalies associated with the MJO are not only zonally extensive but also extend meridionally into the subtropics and extratropics. The subtropical signal is robust, but the extratropical signal, while being statistically significant, is often overwhelmed by in-situ mid-latitude variability. Subtropical circulation anomalies appear more directly linked to the diabatic forcing

associated with the MJO convection anomalies. These anomalies can be isolated through composite studies and in many respects resemble perturbations of the climatological stationary waves.

The MJO may also influence the variance statistics of the circulation through organizing or modulating submonthly variability. This type of influence is more difficult to characterize since it involves Rossby wave dispersion, cold surges, jet streaks, etc., all of which are ubiquitous features of the circulation. We have focused primarily on the first type, although studies of the second type have also been performed.

The composite MJO circulation anomalies have both asymmetric and symmetric components. The symmetric component is largest in the tropics and produces a signal in global atmospheric angular momentum (AAM). Approximately 30-40% of the OLR variance over the IndoPacific warm pool is coherent with length-of-day or global AAM in the 30-70 day band. For the zonal mean the coherent AAM signal is characterized by meridional movement of zonal winds from equatorial regions to the subtropics. Studies of an individual case suggested that the movement is produced by momentum transports and that the frictional torque occurs partially as a response to the transports. **Fig. 3.8**, taken from a composite study, confirms that the covariance between the 30-70 day filtered perturbations and the climatological flow produces the bulk of the

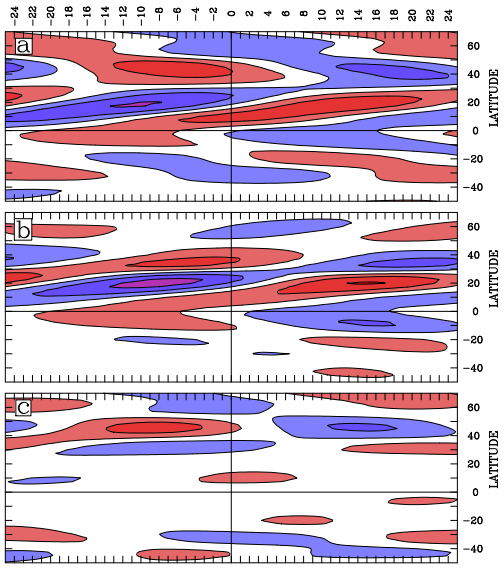

Fig. 3.8. The zonal mean flux convergence of zonal momentum at 200 mb when regressed onto the 30-70-day filtered global relative AAM tendency. The anomalies are for a one standard deviation anomaly in global AAM tendency (=8.0 Hadleys). The abscissa represents leads and lags from -25 to +25 days and the ordinate represents latitude ranging from 70˚N to 50˚S. The contour interval is 0.2 m s^{-1} day^{-1} and positive values ≥ 0.1 m s^{-1} day^{-1} are shaded red, negative values ≤ -0.1 m s^{-1} day^{-1} are shaded blue. The fields have been spectrally truncated to T31. a) the total flux convergence of zonal momentum, b) the portion of the total flux convergence due to the spatial covariance between 30-70 day filtered 200 mb vector wind perturbations and the November-March climatological 200 mb vector wind, c) the difference (a minus b).

momentum transports that give rise to poleward movement of AAM anomalies. There is also a nonlinear component (**Fig. 3.8c**) which suggests that MJO tropical convection could initiate a low or high zonal index state which then persists through an extratropical eddy feedback.

As noted in the previous subsection, enhanced submonthly convective activity accompanies the MJO convective envelope. A similar envelope of enhanced or organized submonthly activity related to cold surges, westerlywind bursts, Rossby wavetrains, etc., also accompanies the

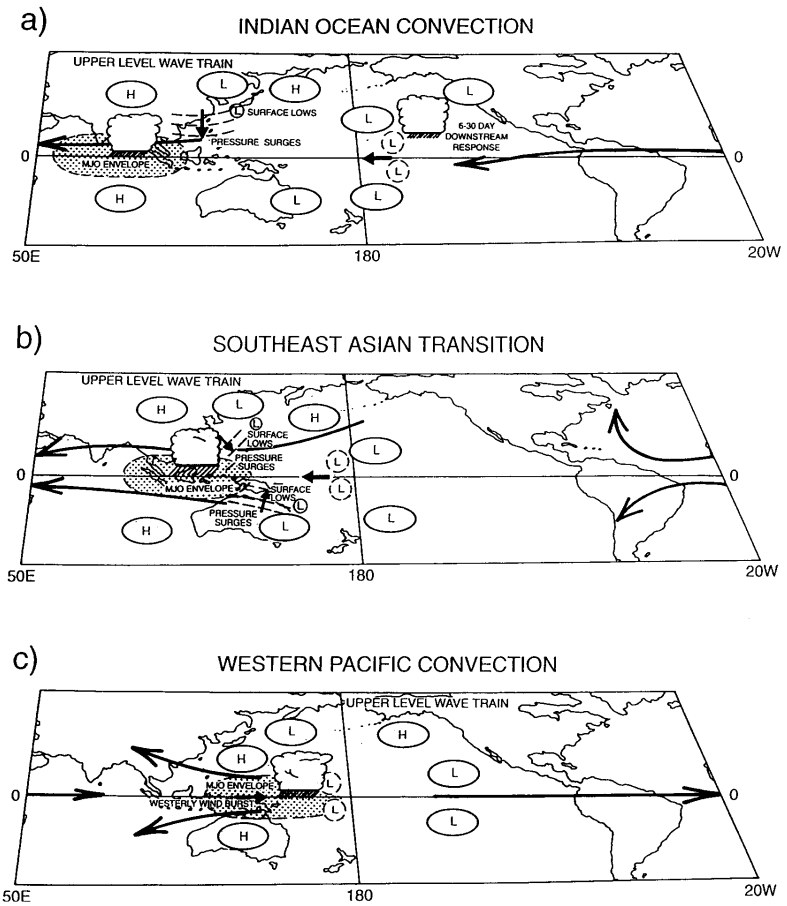

Fig. 3.9. Schematic diagram of time and space scale interactions in the transition of a maximum of convective activity (stippled area) from (a) the eastern Indian Ocean, (b) across Southeast Asia, and (c) into the western equatorial Pacific. To give an example of the timescale, this transition occurred over about a 3-week period in the December 1992 case study described in the text. The H and L in ellipses indicate upper tropospheric circulation anomalies depicting major features of the 6-30 and MJO timescales. The L in dashed circles near the equator denotes westward moving equatorial Rossby waves. L in solid circles indicates surface low-pressure areas. Thick solid arrows represent major features of anomalous upper tropospheric winds. Thin dashed lines near Australia and eastern Asia denote pressure surges.

MJO. **Fig. 3.9** shows a schematic example of some of this activity, based on regression analysis and case studies of individual events.

3.2.3 Equatorial Pacific Ocean dynamics

Equatorial Kelvin waves play a prominent role in both ENSO and the annual cycle of the thermal structure of the eastern Pacific. On sub-annual time scales, intraseasonal Kelvin waves with wavelengths comparable to the width of the Pacific basin and period near 70 days dominate the variability of the equatorial Pacific thermocline. Recent studies have shown that these waves are predominantly forced by eastward propagating zonal wind stress anomalies across the western portion of the Pacific basin, associated with the lower-frequency components of the atmospheric MJO (**Fig. 3.10**). The similar phase speed of the atmospheric MJO (3-5 m/s) and gravest Kelvin wave (~2.3 m/s) results in near-resonant forcing of the Kelvin waves across the western Pacific. Such near-resonant forcing implies that relatively weak surface wind anomalies associated with the MJO are capable of

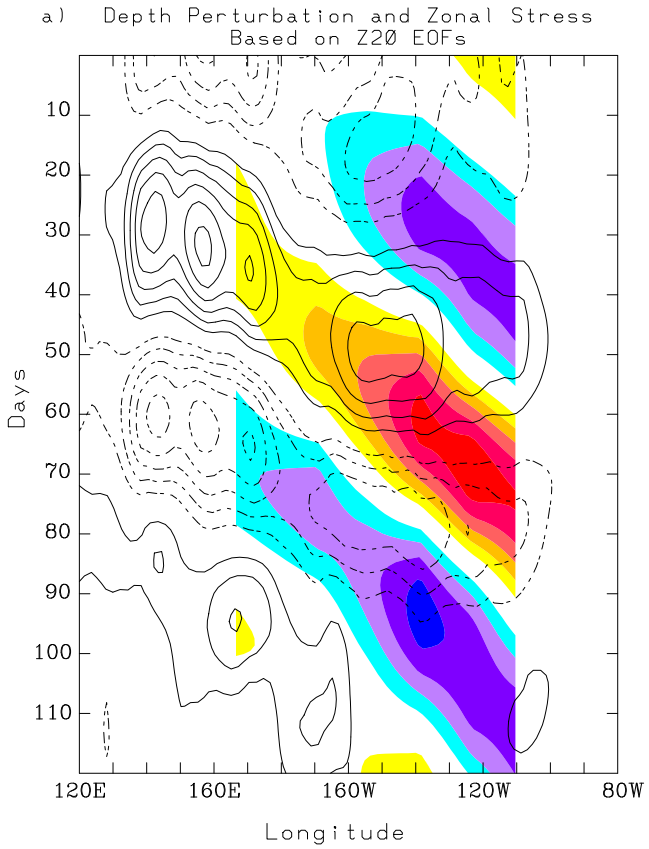

Fig. 3.10. Lagged-regression of Z20 (shading) and zonal stress (contours) onto the principal components of the two leading EOFs of intraseasonally filtered Z20. The regressions are shown along the equator and are scaled for 1.5 standard deviation of the principal components. The shading levels are at 4 m intervals, with dark shades representing positive anomalies. The contour interval for stress is 2.5 x 10^{-3} Nm^{-2} with the zero contour suppressed.

producing relatively large amplitude Kelvin waves.

The intraseasonal Kelvin waves are of fundamental importance for the tropical climate because they produce SST anomalies along the equator via zonal advection and suppression of the thermocline. The possibility of feedback between the zonal extent of the forcing, amplitude of the resultant Kelvin waves, and eastward extent of the warm pool has been proposed (**Fig. 3.11**). Such a mechanism may operate at the onset of some warm ENSO events. A recent example is described in section 3.4.

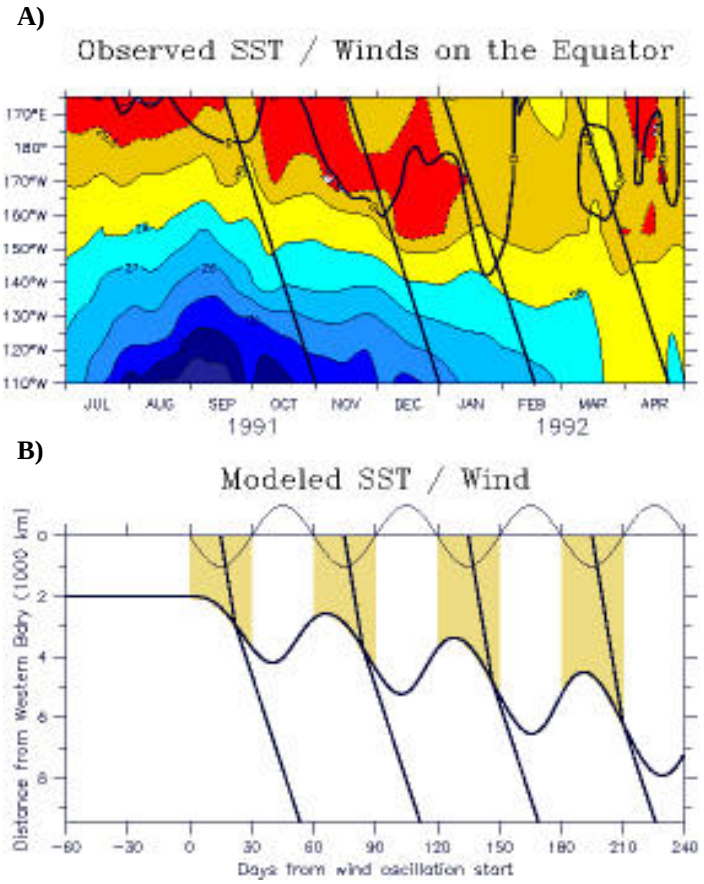

Fig. 3.11. (a) Detail of SST on the equator for July 1991 through April 1992 (during the peak of the El Niño of 1991-1992). Contours and shading show SST with a contour interval of 1˚C, with supplemental contour/shade at 29.5 ˚C. The heavy slant lines are Kelvin wave ray paths from TOGA-TAO data. The heavy contour labeled "0" is the zero line of zonal winds, showing the steplike progression of westerlies eastward over the Pacific during the onset of the warm event. (b) Model SST/wind output from a simple coupled model. The heavy curve is the eastern edge of the 29˚C SST and the wind patch. The light sinusoidal curve at top is the time series of winds from (1) (up is easterly, down is westerly) (winds are zero before day 0). The shading shows the region of westerly winds. Slant lines indicate maximum positive pressure perturbation to match the observed Kelvin lines in Fig. 3.11a; east of the forced region these are Kelvin characteristics, within the forced region they move at speed 2c.

3.2.4 Warm pool sea surface temperatures.

The Coupled Ocean Atmosphere Response Experiment (COARE), conducted in the equatorial western Pacific November 1992-March 1993, highlighted the intraseasonal variation of SST that occurs across the warm pool in conjunction with the atmospheric MJO. Large events, such as occurred in COARE, produce swings in SST of greater than 1˚C with spatial coherence of thousands of kilometers. Such subseasonal SST anomalies in the warm pool are larger than those produced during ENSO or even by the annual cycle. Ongoing research at CDC is focused on understanding the causes of these anomalies and on exploring their impact on intraseasonal and longer time-scale global climate anomalies.

Insight into the mechanism of the MJO and its interaction with the ocean has been gained by developing the relationship between the surface fluxes of heat and momentum and the convective and circulation anomalies associated with the MJO (**Fig. 3.12**). Enhanced latent heat flux, which results from anomalous surface westerlies, lags enhanced convection by about 1 week. Such a phasing suggests that the MJO convective activity is not in quasi-equilibrium with the surface flux of moisture and sensible

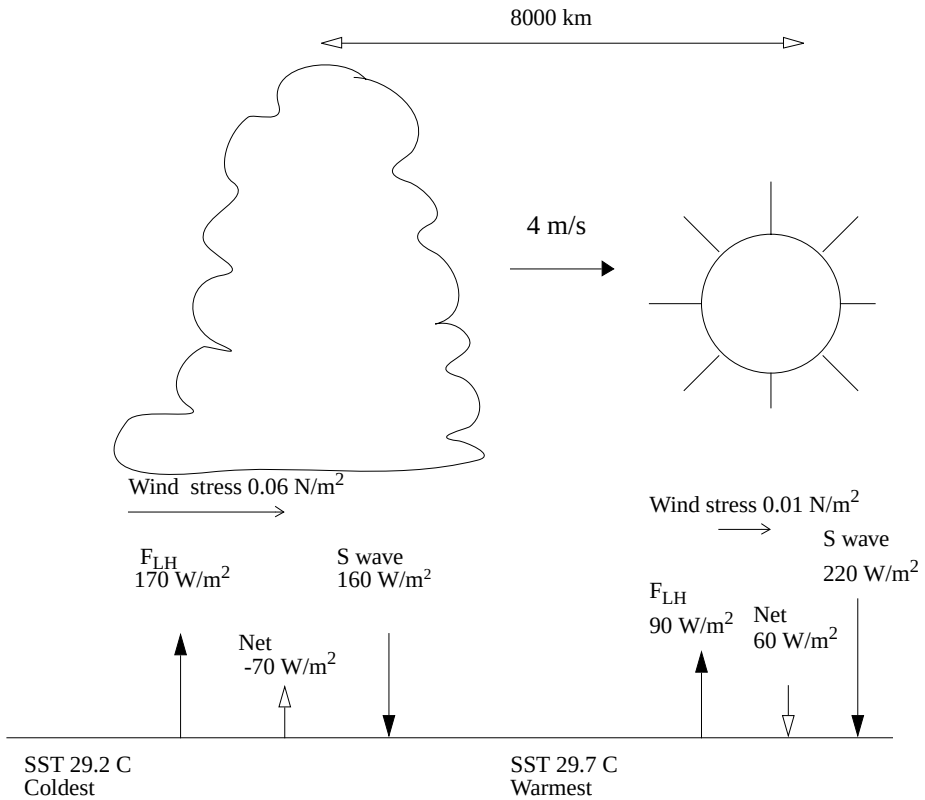

Fig. 3.12. Schematic diagram showing the phase relationship of heat fluxes, convection and SST for intraseasonal oscillations. Typical values of surface fluxes and SST in the western Pacific are shown.

heat. The total surface heat flux (including shortwave radiation) is, however, sufficiently large to drive SST anomalies, which may play an active role in the evolution of the MJO.

A composite evolution of the surface heat flux and SST anomalies that are produced by the MJO was developed (**Fig. 3.13)**. Coherent SST and heat flux anomalies, with a local zonal wavenumber 2 structure, systematically propagate from the Indian Ocean eastward to about the date line. Warm SST lags positive heat flux into the ocean by about 1/4 cycle (10-15 days). The heat flux anomalies result primarily from insolation anomalies associated with cloudiness variations and latent heat flux anomalies produced by surface windspeed variations. Integration of a mixed layer model forced with observed heat flux and wind stress variations (**Fig. 3.13b**) indicate that the intraseasonal SST variations in the warm pool are well explained by one dimensional mixed layer physics. Ongoing research is aimed at understanding the impact of

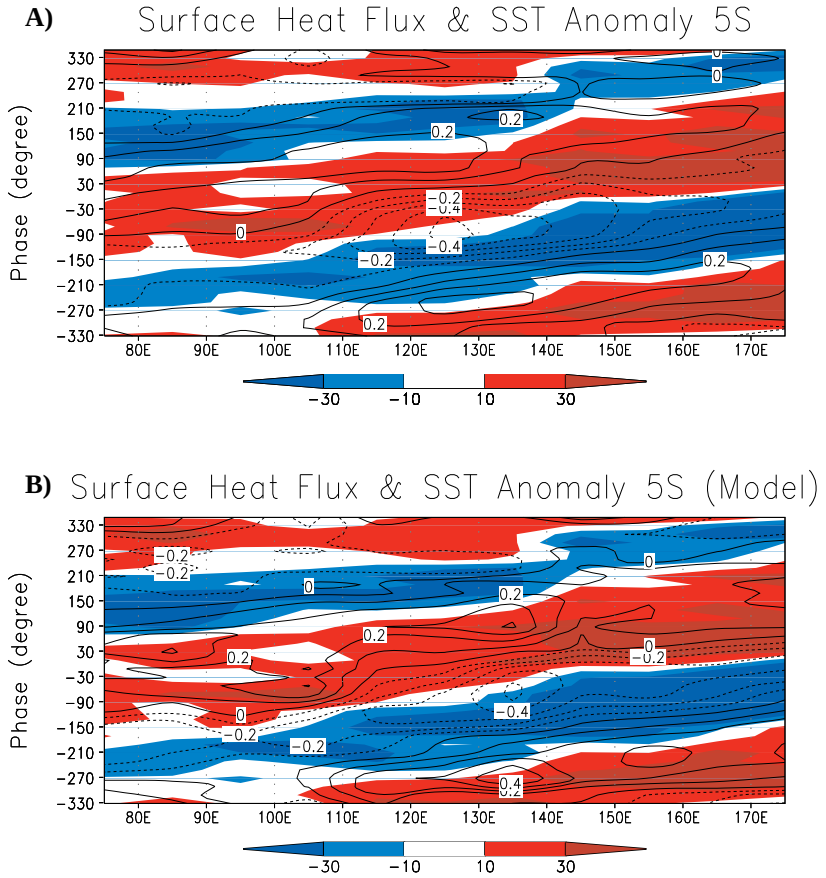

Fig. 3.13. Composite SST anomaly (line contour) from (a) the data (Reynolds and Smith, 1994) and (b) the mixed layer model averaged over 2.5˚ S - 7.5˚ S. Shading indicates net surface heat flux anomaly calculated from (a) the observed SST (Reynolds and Smith, 1994) and (b) the model SST. The vertical axis indicates the phase of intraseasonal oscillations obtained from the EOF analysis of OLR data. A linear trend along the phase axis is eliminated.

these SST variations on large-scale convective activity over the warm pool.

3.2.5 Extratropical sea surface temperature

Unlike the situation in the tropics, the degree to which the *extra-tropical* atmosphere and ocean mutually interact to produce climate anomalies on seasonal-to-interannual time scales is a subject of intense debate. In an effort to shed light on the issue of cause and effect in mid-latitudes, weekly SST and atmospheric circulation data were used to investigate the relative strength of air-sea coupling as a function of time lag. **Table 3.1** shows the total squared covariance between SST and 500 mb heights over the North Atlantic as a function of time lag in weeks. The lag covariances are based on data from 14 winters containing 25 weeks each. Evidently, the air-sea coupling is strongest when the atmosphere leads SST by 2-3 weeks: twice as strong as the simultaneous covariability, and nearly four times as large as when SST leads the atmosphere by a few weeks. This result strongly suggests that the dominant direction of interaction on seasonal-to-interannual time scales in the extra-tropics is that of the atmosphere forcing the ocean. The maximization of air-sea coupling when the atmosphere leads SST by 2-3 weeks is consistent with the theoretical stochastic atmospheric forcing model of Frankignoul and Hasselmann [*Tellus*, **29**, 357(1977)], in which the ocean mixed layer responds passively to high-frequency stochastic atmospheric forcing.

A GFDL GCM simulation has been used to study the surface flux variability over the North Pacific and Atlantic Oceans during winter. The surface flux anomalies are organized by the low-level atmospheric circulation in agreement with previous observational studies. Surface flux variability in the 3-10 day time band is clearly associated with midlatitude storms. The SLP and surface flux anomalies are also strong in the 10-30 day band but are located further north, are broader in scale, and propagate ~3-4 times more slowly eastward than the synoptic disturbances. More than half of the variability occurs on submonthly timescales. The anomalous wind speed has the greatest influence on surface flux anomalies in the subtropics and western Pacific, while the flux anomalies are more closely

Table 3.1. Total temporal squared covariance between normalized SST and 500-mb height anomalies over the North Atlantic during winter as a function of lag in weeks. Negative (positive) lags indicate SST leads (lags) the atmosphere. Units are non-dimensional as each grid point has been normalized by its respective standard deviation. The simultaneous covariance has been arbitrarily assigned a value of 100 units. (Top row) Unfiltered data; (bottom row) intraseasonal data.

	Lag in weeks								
	-4	**-3**	**-2**	**-1**	**0**	**1**	**2**	**3**	**4**
Unf	53	51	51	64	100	141	159	155	140
Intra	62	59	52	57	100	158	176	164	136

associated with air temperature and moisture anomalies in the northeast Pacific and over the Atlantic north of 40˚N.

3.2.6 Dynamical initiation of droughts.

Much of the contiguous United States experienced severe hot and dry conditions during the summers of 1980 and 1988. Overall damages to the society and environment made the 1988 drought one of the nation's greatest disasters of the twentieth century.

We have compared the relative roles of remote and local forcing in the evolutions of the extreme U.S. summer heat wave-droughts of 1980 and 1988. The results indicate the importance of both dynamical forcing from remote sources and anomalous local boundary conditions in accounting for the two extreme heat wave-droughts. The relative importance of these factors varies significantly during the evolution of the events. In at least these two cases, the evolution of extreme heat wave-droughts can be interpreted as a two-stage process, with large-scale dynamical processes playing the key role in initiating the droughts, and local surface feedbacks assuming a major role in their persistence.

The nature of the remote forcing of drought is under debate. Trenberth et al. [*Science*, **242**, 1640(1988)] has proposed that the primary cause of the 1988 drought was the strong anomalous upper-level anticyclone over the Great Plains in the April-May-June (AMJ) mean. They further suggested that this anomalous upper-level anticyclone was part of a tropically forced stationary wave train extending from the southeastern North Pacific to over North America. However, closer examination of the evolution of the upper-tropospheric circulation suggests that the 1988 AMJ seasonal mean may not accurately represent atmospheric conditions during the drought. For example, **Fig. 3.14** shows a time-longitude plot of 10-day lowpass streamfunction anomalies averaged between 30˚N and 60˚N. Over the North America region (e.g., longitudes 60˚W-135˚W) the circulation

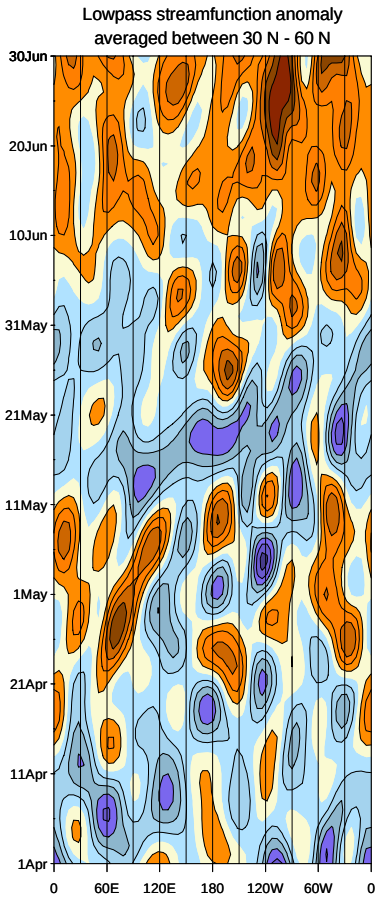

Fig. 3.14 Time-longitude plot of observed 200 mb 10-day lowpass streamfunction anomalies averaged over the latitude belt from 30˚N to 60˚N for 1 April 1988-30 June 1988. The contour interval is 4 x 10^6 m^2s^{-1}; negative values are shaded blue.

exhibited substantial intraseasonal variation throughout the spring. Two strong anomalous anticyclones in early and late June are evident; these dominate the AMJ mean. In April and May, not only were there no persistent anomalous anticyclones over North America, but a pronounced negative streamfunction anomaly existed during mid-May.

Synoptic maps of lowpass streamfunction during this time suggest the presence of energy propagation across the Pacific in the first half of May and in early June. Furthermore, the rapid development of the large anticyclones over North America during June was preceeded by large OLR anomalies over the west Pacific, but not over the eastern tropical Pacific. These observations, along with results from a barotropic model forced by observed divergence anomalies, strongly suggest that downstream energy propagation of Rossby waves forced over Southeast Asia and the west Pacific was primarily responsible for the rapid development during June of the two anomalous anticyclones over the Great Plains.

In sum, work done at CDC indicates that drought may be better studied not as a single, steady seasonal event, but rather as a succession of events that together produce a serious hydrological deficit. These results have significant implications for the factors necessary to simulate and predict the evolution of severe large-scale droughts. The extent to which these events are deterministically influenced by boundary forcing (both due to anomalous SST and soil moisture feedbacks), and the extent to which they arise from natural variability of the tropics/extratropics, are topics of ongoing research at CDC.

3.3 Use and evaluation of the NCAR/NCEP reanalysis

CDC makes considerable use of the NCAR/NCEP reanalysis both for research and climate monitoring. Many of the projects described in this and other chapters use the reanalysis in one way or another. Projects are also underway to evaluate the reanalysis and to use some of its unique components such as the diabatic heating fields and the σ-level data.

3.3.1 Atmospheric budgets

The σ-level data provides an opportunity to compute atmospheric budgets that are in the assimilating model's coordinates and thus free of interpolation errors. Work has begun on examining atmospheric angular momentum (AAM), absolute vorticity and potential vorticity budgets. Applications have ranged from determining at which level (if any) an equivalent barotropic model can be applied, to dynamically adjusting the analyzed divergence, to explaining the vertically-integrated AAM tendency. There are substantial residuals in some of these budgets. As an example, **Fig. 3.15** shows the zonal and global AAM tendency associated with the annual cycle during 1979-95. The observed tendency (**Fig. 3.15a**) along with two calculated tendencies based on the NCEP operational analysis (**Fig. 3.15b**) and NCEP reanalysis (**Fig. 3.15c**) are displayed. If the budgets were perfectly balanced, all three figures would be identical. However, this is not the case

in either the operational nor the reanalysis tendency. Using the NCEP reanalysis, this sensitive budget has a global residual of -15 Hadleys, which would spin down the global relative AAM to zero in ~120 days. The zonal structure of the imbalance (contours in **Fig. 3.15c**) suggests that either the NCEP surface stresses are too weak or that the momentum transports are too strong. The use of 6-hour forecasts of the surface stress to compute the friction torque leads us to suspect the predicted stresses. This could be tested with a "one-time step" approach applied to the initial conditions from the reanalysis.

3.3.2 Surface heat fluxes

Several projects are underway to evaluate the surface heat fluxes in the reanalysis. In section 3.1.1, large discrepancies in the annual harmonic of the NCEP radiative surface flux were documented. Similar problems in the surface short wave flux were found when comparing the reanalysis to in-situ observations from the tropical west Pacific. NCEP clouds appear to be the primary cause for these differences. On the other hand, evaporative fluxes agreed favorably with in-situ tropical observations.

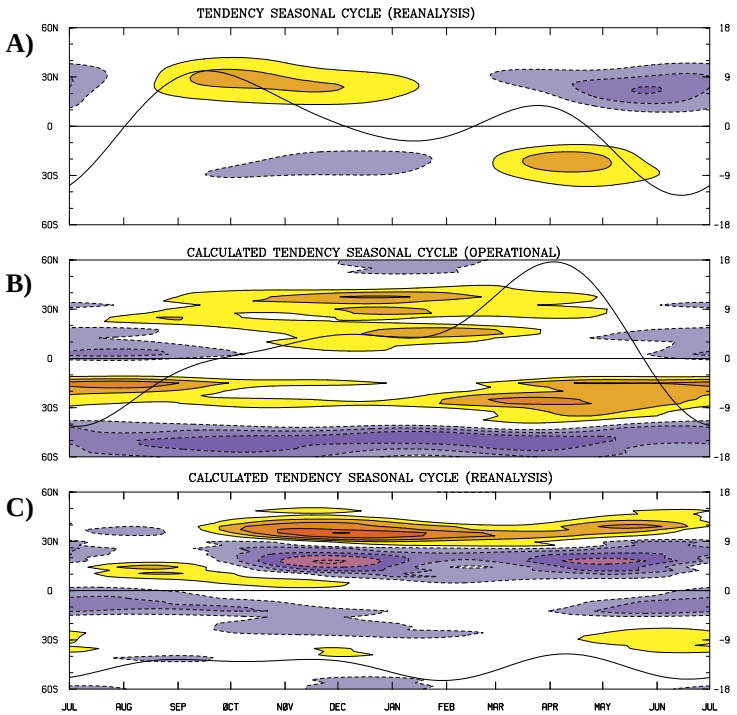

Fig. 3.15 Latitude-time plot of atmospheric angular momentum tendency for the 1979-95 annual cycle (first three harmonics): a) the observed tendency based on NCAR/NCEP reanalysis, b) the calculated tendency based on NMC operational momentum fluxes and torques and c) the calculated tendency based on NCAR/NCEP reanalysis momentum fluxes and torques. All three panels show zonal integrals: a) is contoured with an interval of 0.2.Hadleys/degree of latitude (1 Hadley=1.0×10^{18} kg m^2 s^{-2}) while b) and c) have an interval of 0.4 Hadleys/degree. Data are daily and time runs from 1 July at the left edge to 1 July on the right. The curve on each panel is the global AAM tendency and its scale is shown on the right; the labels are in Hadleys.

In mid-latitudes, the 4-week SST tendency, and the tendency resulting from the reanalysis sensible and latent energy fluxes using climatological mixed layer depths were compared in both the N. Pacific and N. Atlantic. The two spatial patterns are nearly identical, and the magnitudes are close: the fluxes induce about two-thirds of the observed SST tendencies. Thus during northern winter, when the short wave flux is less important, the NCEP surface fluxes appear useful for studying weekly SST tendencies and perhaps the re-emergence of SST anomalies discussed in section 3.1.3.

3.3.3 Diabatic heating

The three-dimensional diabatic heating fields are a valuable resource for a variety of climate and weather applications. The fields have been used to force baroclinic models, study three-dimensional transports and compare with GCM heating rates and profiles.

Diagnostics computed from the NCEP and the NASA diabatic heating rates have been compared to obtain a lower bound on uncertainty in these fields. Of particular interest are the terms in the potential vorticity budget that are related to tropical diabatic heating. In addition, the dynamical significance of these uncertainties is examined by computing the linear steady solution of a baroclinic model forced by the difference between the NCEP and NASA heating rates.

The heating rates are also being regressed onto sea surface temperatures to provide fields to force steady baroclinic models and to compare with GCM-produced heating. These data will be used to study ENSO-induced circulation anomalies and their sensitivity to SST.

3.3.4 Divergence

Another sensitive quantity is the tropical upper tropospheric divergence, whose horizontal distribution closely follows that of the column-integrated diabatic heating. The divergence also plays a direct role in tropical-extratropical interactions. There are reasons to believe that the 200 mb divergence in the NCEP reanalyses has some serious biases, and is inconsistent with the 200 mb vorticity budget.

CDC scientists have developed a method of making minimal modifications to wind fields so that they satisfy the vorticity budget. The procedure involves solving the so-called "generalized chi problem". **Fig. 3.16** shows a 13-winter (DJF 1980-93) average of the 200 mb divergence in the NCEP reanalyses (labeled 'pre-chi'), the minimally modified NCEP reanalyses (labeled 'post-chi'), the operational ECMWF analyses ('pre-chi'), and the minimally modified ECMWF analyses ('post-chi'). The figure also shows the 13-winter averages of OLR and precipitation. The NCEP 'pre-chi' reanalysis field is in several ways the outlier among these six fields. Of particular concern is the large divergence over the western north equatorial Pacific ocean, which is considerably weaker in the 'post-chi' NCEP field (even with the minimal modification), and absent in all the other fields. Ongoing work is focused on identifying the sources for these discrepancies.

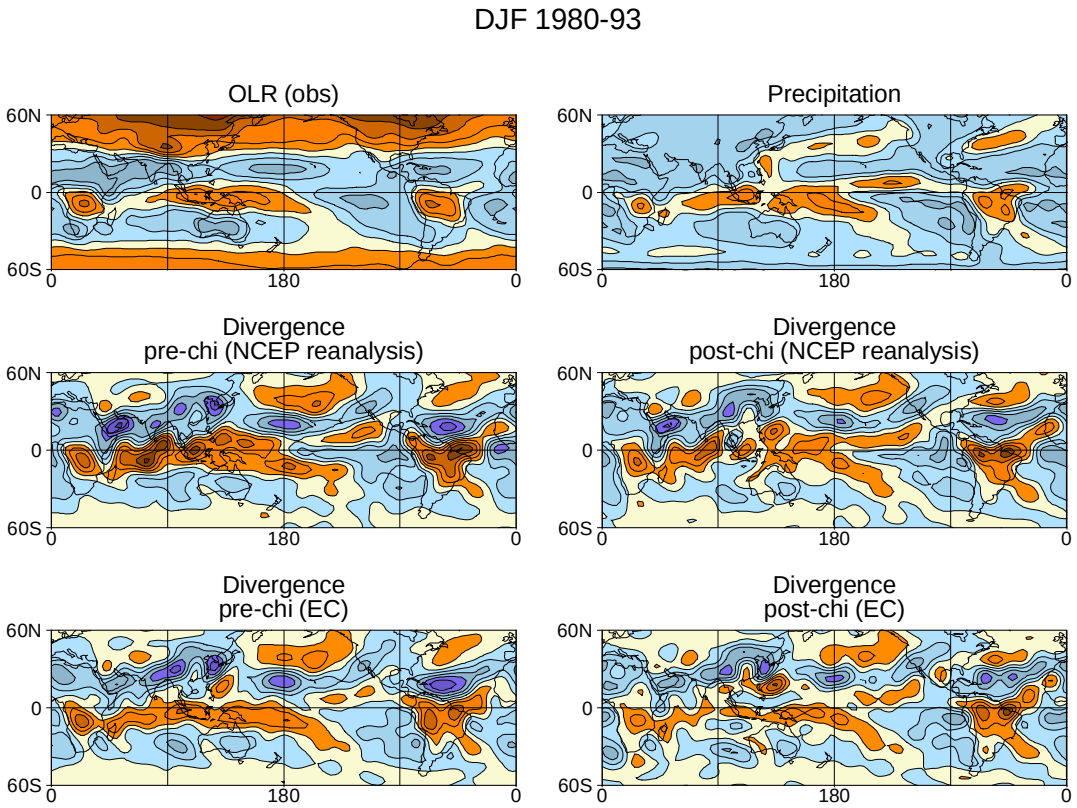

Figure 3.16 December-January-February averages for the years 1980-93 for four divergence fields and an outgoing longwave radiation and precipitation field.

3.4 Real time monitoring

In this section a real time climate situation is discussed to illustrate processes and phenomena which are being investigated and monitored at CDC. **Fig. 3.17** shows a time-longitude diagram of normalized 3-month running mean SST anomalies for the last 15 years. The most prominent feature is the ENSO cycle. A less distinctive but robust feature is the eastward movement of positive SST anomalies from the western Pacific toward the dateline. In some cases the eastward expansion is brief (1989-90, 1990-91, 1995-96) whereas in others it precedes the basin-wide warming associated with ENSO.

Real time monitoring indicates that the expansion occurs in steps associated with MJOs and this is confirmed by diagnostics of the 1979-97 period. As of this writing, a well-defined expansion is underway during the 1996-97 northern winter. The link with MJOs can be seen in **Fig. 3.18** which shows the OLR field in a time-longitude format. Three MJOs are evident between October and March in the 60˚E to 180˚ longitude band. The convective signal for each succeeding MJO is farther east than the previous one. One mechanism that can account for this behavior is zonal temperature advection by the oceanic Kelvin wave forced by MJO winds. A simple illustra-

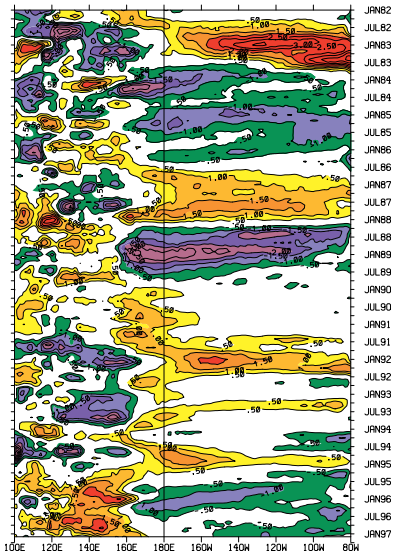

Fig. 3.17. Longitude-time plot of normalized sea surface temperature anomalies averaged between 4˚N-4˚S. Yellow/red (green/blue) shading represents positive (negative) standard deviations. The contour interval is 0.5 standard deviations. The data are weekly and have been smoothed with a 13-week running mean.

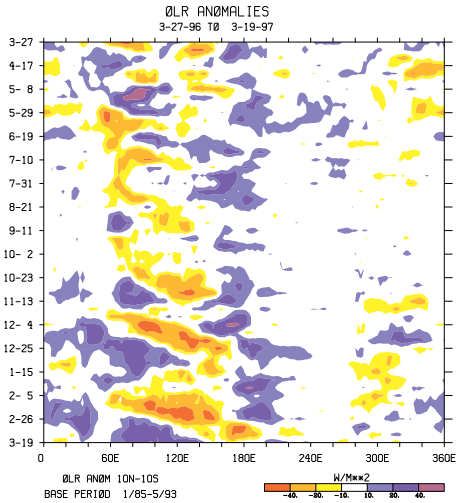

Fig. 3.18. Longitude-time plot of outgoing longwave radiation anomalies (OLR) averaged between 10˚N-10˚S. Yellow/red (blue/purple) shading represents negative (positive) OLR anomalies. Negative OLR anomalies correspond to positive deep convection anomalies. Data are weekly and the labels on the ordinate represent the middle of the week.

tion of the mechanism was presented in **Fig. 3.11**.

The MJOs are also associated with global changes in the atmospheric circulation. **Fig. 3.19** shows the zonal and global AAM anomalies for the period April 1996 to March 1997. The global AAM contains some large AAM oscillations at the end of the period that coincide with the last two MJOs seen in **Fig. 3.18**. These contrast with the relatively weak increase in AAM that accompanied the MJO during October-November 1996. However, all three MJOs are associated with positive zonal AAM anomalies in the tropics (**Fig. 3.19**, top) much as described in section 3.2.2. The different behavior in the last two events could be related to the initiation of a zonal-eddy feedback that maintains the existing phase of the zonal index and possibly even influences the MJO.

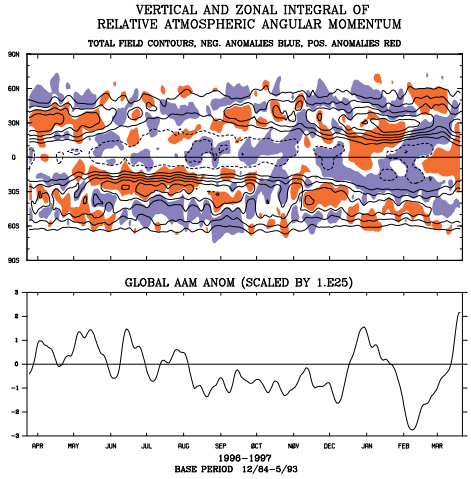

Fig. 3.19. Top) Time-latitude plot of zonal integral of atmospheric angular momentum (AAM): total AAM is contoured with an interval of 2.0×10^{24} kgm^2s^{-1} and no zero contour, AAM anomalies are shaded red (blue) for anomalies 2.0×10^{24} kgm^2s^{-1} ($\leq 2.0 \times 10^{24}$ kgm^2s^{-1}). Bottom) line plot of global AAM anomaly. Data in both panels are daily and have been smoothed with a 5-day running mean.

Contributed by: *K. Weickmann, M. Alexander, J. Bergman, P. Chen, C. Deser, R. Dole, H. Hendon, B. Liebmann, B. Mapes, M. Newman, P. Sardeshmukh, T. Shinoda, and J. Whitaker.*

References:

Journal Articles

Bergman, J. W. and M. L. Salby 1994: Equatorial wave activity calculated from observed convective activity. *J. Atmos. Sci*, **51**,3791-3806 .

Bergman, J. W. and M. L. Salby 1996: Diurnal variations of cloud cover and their relationship to climatological conditions. *J. Climate*, **9**,2802-2820.

Chen, P. 1995: Isentropic cross-tropopause mass exchange in the extratropics. *J. Geophys. Res.*, **100**,16661-16673.

Chen, P. 1996: The influences of zonal flow on wavebreaking and Tropical/extratropical interaction in the lower stratosphere. *J. Atmos. Sci.*, **53**,2379-2392.

Deser, C. and M. S. Timlin 1997: Atmosphere-Ocean Interaction on weekly time scales in the North Atlantic and Pacific. *J. Climate*, **10**, 393-408.

Gutzler, D., G. Kiladis, G. Meehl, K. Weickmann and M. Wheeler 1994: The global climate of December 1992-February 1993. Part II. Large-scale variability across the tropical western Pacific during TOGA COARE. *J. Climate* , **7**,1606-1622.

Hendon, H. H. and M. L. Salby 1994: Life cycle of the the Madden Julian oscillation. *J. Atmos. Sci.*, **51**,2225-2237.

Hendon, H. H. and B. Liebmann 1994: Organization of convection within the Madden-Julian Oscillation. *J. Geophys. Res.*, **99**,8073-8083.

Hendon, H. H. 1995: Length of day fluctuations associated with the Madden Julian oscillation. *J. Atmos. Sci.*, **52**,2373-2383.

Hendon, H. H. and M. L. Salby 1996: Planetary-scale circulations forced by intraseasonal variations of observed convection. *J. Atmos. Sci.*, **53**,1751-1758.

Hendon, H. H. and J. Glick 1997: Intraseasonal air-sea interaction in the tropical Indian and western Pacific Oceans. *J. Climate*, **10**,647-661.

Kessler, W., M. McPhaden and K. Weickmann 1995: Forcing of intraseasonal Kelvin waves in the equatorial Pacific. *J. Geophys. Res.*, **100**,10613-10631.

Kiladis, G., G. Meehl and K. Weickmann 1994: The large scale circulation associated with westerly wind bursts and deep convection over the western equatorial Pacific. *J. Geophys. Res.*, **99**,18527-18544.

Liebmann, B. and C. A. Smith 1996: Description of a complete (interpolated) outgoing longwave radiation dataset. *Bull. Amer. Meteor. Soc.*, **77**,1275-1277.

Lyon, B. F. and R. M. Dole 1995: A comparative study of the intense summer heat wave/droughts of 1980 and 1988. *J. Climate*, **8**,1658-1676.

Mapes, B. E. 1993: Gregarious tropical convection. *J. Atmos. Sci.*, **50**,2026-2037.

Mapes, B. E. and R. A. Houze, Jr. 1993: Cloud clusters and superclusters over the oceanic warm pool. *Mon. Wea. Rev.*, **121**,1398-1415.

Mapes, B. E. and R. A. Houze, Jr. 1993: An integrated view of the 1987 Australian monsoon and its mesoscale convective systems. Part II: Vertical structure. *Quart. J. Roy. Meteor. Soc.*, **119**,733-754.

Mapes, B. E. and R. A. Houze, Jr. 1995: Diabatic divergence profiles in tropical mesoscale convective systems. *J. Atmos. Sci.*, **52**,1807-1828.

Mapes, B. E. and P. Zuidema 1996: Radiative-dynamical consequences of dry tongues in the tropical troposphere. *J. Atmos. Sci.*, **53**,620-638.

Meehl, G., G. Kiladis, K. Weickmann, M. Wheeler, D. Gutzler and G. Compo 1996: Modulation of equatorial subseasonal convective episodes by tropical-extratropical interaction in the Indian and Pacific Ocean regions. *J. Geophys. Res.*, **101**,15033-15049.

Newman, M. and P. D. Sardeshmukh 1995: A caveat concerning Singular Value Decomposition. *J. Climate*, **8**,352-360.

Salby, M. L., R. Garcia and H. H. Hendon 1994: Planetary circulations in the presence of climatological and wave induced heating. *J. Atmos. Sci.*, **51**,2344-2367.

Salby, M. L. and H. H. Hendon 1994: Intraseasonal behavior of winds, temperature and convection in the tropics. *J. Atmos. Sci.*, **51**,2207-2224.

Sardeshmukh, P. D. 1993: The baroclinic chi problem and its application to the diagnosis of atmospheric heating rates. *J. Atmos. Sci.*, **50**,1099-1112.

Weickmann, K. and P. Sardeshmukh 1994: The atmospheric angular momentum budget associated with a Madden-Julian Oscillation. *J. Atmos. Sci.*, **51**,3194-3208.

Submitted or in Press

Alexander, M. A. and J. D. Scott 1996: Surface flux variability over the North Pacific and North Atlantic Oceans. *J. Climate*, **submitted.**

Bergman, J. W. 1997: A numerical investigation of cloud diurnal variations. *J. Climate*, **submitted**.

Bergman, J. W. and M. L. Salby 1997: The role of cloud diurnal variations in the time-mean energy budget. *J. Climate*, **in press**.

Chen, P. and M. Newman 1996: Rossby-wave propagation and the rapid development of upper-level anomalous anticyclones during the 1988 U.S. drought. *J. Climate*, **submitted**

Chen, P. 1997: Asymmetries and abrupt changes in the annual cycle of the Asian and American jet streams. *J. Climate*, **submitted**.

Hendon, H. H., B. Liebmann and J. D. Glick 1997: Oceanic Kelvin waves and the Madden Julian oscillation. *J. Atmos. Sci.*, **submitted**.

Liebmann, B., H. H. Hendon and J. D. Glick 1997: The role of the diurnal cycle in generating two-day convective disturbances. *J. Meteor. Soc. Japan*, **in revision**.

Kiladis, G. N. and K. M. Weickmann 1997: Horizontal structure and seasonality of large-scale circulations associated with submonthly tropical convection. *Mon. Wea. Rev.*, **125**, **in press**.

Mapes, B. E. 1997: The large-scale part of tropical mesoscale convective system circulations: a linear vertical spectral band model. *J. Meteor. Soc. Japan*, **in review**.

Mapes, B. E. 1997: Equilibrium vs. activation controls on large-scale variations of tropical deep convection. *The physics and parameterization of moist convection*, NATO-ASI **in press.**

Mapes, B. E. 1997: Mutual adjustment of mass flux and stratification profiles. *The physics and parameterization of moist convection*, NATO-ASI **in press**.

Weickmann, K., G. Kiladis and P. Sardeshmukh 1997: The dynamics of intraseasonal atmospheric angular momentum oscillations. *J. Atmos. Sci.*, **in press**.

This page intentionally left blank.